

# Dual-energy CT quantitative imaging

Citation for published version (APA):

Almeida, I. P., Schyns, L. E. J. R., Ollers, M. C., van Elmpt, W., Parodi, K., Landry, G., & Verhaegen, F. (2017). Dual-energy CT quantitative imaging: a comparison study between twin-beam and dual-source CT scanners. *Medical Physics*, *44*(1), 171-179. <https://doi.org/10.1002/mp.12000>

## Document status and date:

Published: 01/01/2017

## DOI:

[10.1002/mp.12000](https://doi.org/10.1002/mp.12000)

## Document Version:

Publisher's PDF, also known as Version of record

## Document license:

Taverne

## Please check the document version of this publication:

- A submitted manuscript is the version of the article upon submission and before peer-review. There can be important differences between the submitted version and the official published version of record. People interested in the research are advised to contact the author for the final version of the publication, or visit the DOI to the publisher's website.
- The final author version and the galley proof are versions of the publication after peer review.
- The final published version features the final layout of the paper including the volume, issue and page numbers.

[Link to publication](#)

## General rights

Copyright and moral rights for the publications made accessible in the public portal are retained by the authors and/or other copyright owners and it is a condition of accessing publications that users recognise and abide by the legal requirements associated with these rights.

- Users may download and print one copy of any publication from the public portal for the purpose of private study or research.
- You may not further distribute the material or use it for any profit-making activity or commercial gain
- You may freely distribute the URL identifying the publication in the public portal.

If the publication is distributed under the terms of Article 25fa of the Dutch Copyright Act, indicated by the "Taverne" license above, please follow below link for the End User Agreement:

[www.umlib.nl/taverne-license](http://www.umlib.nl/taverne-license)

## Take down policy

If you believe that this document breaches copyright please contact us at:

[repository@maastrichtuniversity.nl](mailto:repository@maastrichtuniversity.nl)

providing details and we will investigate your claim.

Our Magphan RT family continues to grow to meet QA needs for MR imaging of large fields of view.



The modular design enables the Magphan® RT phantom to be handled by a single person without special equipment. The three-piece configuration measures geometric distortion and uniformity along with tests for laser alignment, slice thickness, resolution, and Signal-to-Noise Ratio. The central section contains 24 contrast spheres that cover a range of T1, T2, and ADC values, as well as two slice thickness ramps.

The Phantom Laboratory manufactures high-precision phantoms coupled with Smári image analysis service and innovative custom solutions for the medical imaging and radiation therapy fields.

---

[Click to view our phantoms and schedule a demo of our Smári image analysis service.](#)

# Dual-energy CT quantitative imaging: a comparison study between twin-beam and dual-source CT scanners

Isabel P. Almeida, Lotte E. J. R. Schyns, Michel C. Öllers, and Wouter van Elmpt  
*Department of Radiation Oncology (MAASTRO), GROW – School for Oncology and Developmental Biology, Maastricht University Medical Centre, Maastricht, The Netherlands*

Katia Parodi and Guillaume Landry  
*Department of Medical Physics, Faculty of Physics, Ludwig-Maximilians-Universität München, Am Coulombwall 1, 85748 Garching b. München, Germany*

Frank Verhaegen<sup>a)</sup>  
*Department of Radiation Oncology (MAASTRO), GROW – School for Oncology and Developmental Biology, Maastricht University Medical Centre, Maastricht, The Netherlands*

(Received 6 July 2016; revised 25 August 2016; accepted for publication 4 November 2016; published 13 January 2017)

**Purpose:** To assess image quality and to quantify the accuracy of relative electron densities ( $\rho_e$ ) and effective atomic numbers ( $Z_{eff}$ ) for three dual-energy computed tomography (DECT) scanners: a novel single-source split-filter (i.e., twin-beam) and two dual-source scanners.

**Methods:** Measurements were made with a second generation dual-source scanner at 80/140Sn kVp, a third-generation twin-beam single-source scanner at 120 kVp with gold (Au) and tin (Sn) filters, and a third-generation dual-source scanner at 90/150Sn kVp. Three phantoms with tissue inserts were scanned and used for calibration and validation of parameterized methods to extract  $\rho_e$  and  $Z_{eff}$ , whereas iodine and calcium inserts were used to quantify Contrast-to-Noise-Ratio (CNR). Spatial resolution in tomographic images was also tested.

**Results:** The third-generation scanners have an image resolution of 6.2,  $\sim 0.5$  lp/cm higher than the second generation scanner. The twin-beam scanner has low imaging contrast for iodine materials due to its limited spectral separation. The parameterization methods resulted in calibrations with low fit residuals for the dual-source scanners, yielding values of  $\rho_e$  and  $Z_{eff}$  close to the reference values (errors within 1.2% for  $\rho_e$  and 6.2% for  $Z_{eff}$  for a dose of 20 mGy, excluding lung substitute tissues). The twin-beam scanner presented overall higher errors (within 3.2% for  $\rho_e$  and 28% for  $Z_{eff}$ , also excluding lung inserts) and also larger variations for uniform inserts.

**Conclusions:** Spatial resolution is similar for the three scanners. The twin-beam is able to derive  $\rho_e$  and  $Z_{eff}$ , but with inferior accuracy compared to both dual-source scanners. © 2016 American Association of Physicists in Medicine [<https://doi.org/10.1002/mp.12000>]

Key words: Dual-energy dual-source CT, Dual-energy twin-beam CT, effective atomic number, relative electron density

## 1. INTRODUCTION

Computed tomography (CT) is a crucial imaging modality for the future developments of quantitative imaging. However, CT numbers depend on the scanner characteristics and on the reconstruction model, meaning that the same material will show different CT numbers if the scanning and reconstruction settings are not the same.<sup>1,2</sup>

Dual-energy computed tomography (DECT) imaging has the potential to improve quantitative imaging by adding a second set of data to the same scanned material.<sup>3</sup> This imaging modality results in two 3-dimensional attenuation maps by scanning with two different photon spectra. Various methods have been described to transform these two sets of data from CT numbers to electron densities relative to water ( $\rho_e$ ) and

effective atomic numbers ( $Z_{eff}$ ),<sup>4–10</sup> quantities suitable for quantitative imaging. The additional  $Z_{eff}$  information allows the distinction of different tissues types that have similar  $\rho_e$ .<sup>11</sup> DECT is not only a powerful technique to obtain material-specific information, but it also reduces beam-hardening artifacts compared with conventional single energy CT (SECT).<sup>12</sup>

Moreover, SECT requires a calibration that is conventionally done with tissue-equivalent materials to obtain the  $\rho_e$  from the CT numbers. Uncertainties arise from the suitability of these tissue-equivalent materials and the number of tissue types needed to have a proper calibration (Fig. 1 from Bazalova et al.<sup>5</sup>). The calibration in DECT is done by phantoms with known  $\rho_e$  and  $Z_{eff}$  values.

Different DECT modalities are commercially available and these are based on single or dual-source CT scanners.<sup>3</sup>

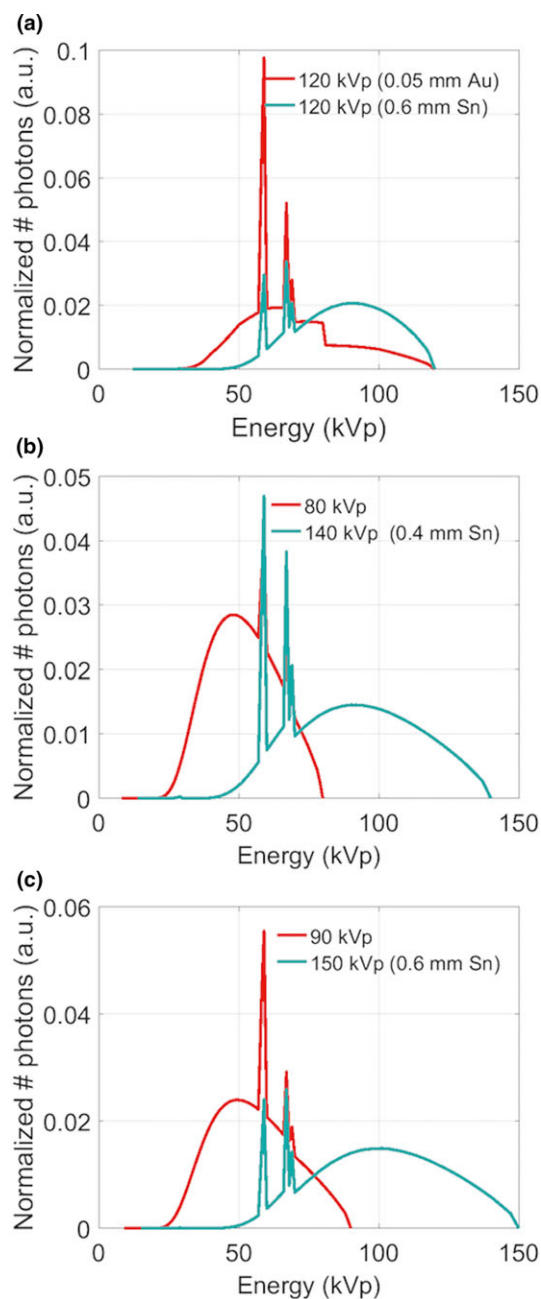


FIG. 1. Normalized X-ray photon spectra used in the EDGE (a), FLASH (b) and FORCE (c) scanners. All high energy spectra have a tin (Sn) filtration (0.6 mm for the EDGE and FORCE and 0.4 mm for the FLASH). The EDGE low energy spectrum has a gold (Au) filter of 0.05 mm. [Color figure can be viewed at [wileyonlinelibrary.com](http://wileyonlinelibrary.com)]

A single-source CT scanner can provide DECT images by performing two consecutive spiral scans at different energies, scanning with a fast kilovolt-switching, using a dual-layer detector system or scanning with a split beam with different filters. The latter is a novel technique where a single beam is split using two filters, which results in two different photon spectra for the same source and thus producing DECT images.<sup>13</sup> Dual-source scanners produce DECT images by using two orthogonal tubes with different filtrations and voltages that can range from 70 kVp to 150 kVp.<sup>14</sup>

The purpose of this study is to assess image quality and to quantify the accuracy of  $\rho_e$  and  $Z_{eff}$  for three DECT scanners: a third-generation single-source twin-beam and two dual-source scanners (second and third generations).

## 2. MATERIALS AND METHODS

### 2.A. CT scanners and image reconstruction

DECT imaging was performed with three DECT scanners (Siemens Healthineers, Forchheim, Germany): a third-generation twin-beam scanner (SOMATOM Definition EDGE), a third-generation dual-source scanner (SOMATOM Definition FORCE) and a second generation dual-source scanner (SOMATOM Definition FLASH). The dual-source scanner FORCE and the twin-beam scanner EDGE were equipped with third-generation digital detectors (Stellar detector, Siemens Healthineers, Forchheim, Germany), which reduce electronic noise (on average by 30%) and cross talk, compared with conventional Ultra-Fast-Ceramic (UFC) solid-state CT detectors<sup>15</sup> used in the FLASH scanner. Table I presents all scanning and reconstruction settings for three dose levels. Reconstructions were performed with filtered back projection (FBP) kernels and with equivalent iterative kernels with strength five.<sup>16</sup> The use of the same settings for the three scanners was not possible due to different software versions that were installed on the different scanners. Figure 1 shows the spectral pairs of each scanner used in this work simulated with the software SpekCalc.<sup>17–19</sup>

### 2.B. Phantoms

A Gammex RMI 467 phantom (Gammex Inc. Middleton, WI, USA) was scanned with two different configurations. First, 16 tissue mimicking inserts (Gammex Inc. Middleton, WI, USA) were placed and scanned in a certain load pattern [Fig. 2(a)], in which bone-equivalent materials are spread out to minimized artifacts. A second scan followed using six iodine and six calcium inserts with different densities (Gammex Inc. Middleton, WI, USA) and the remaining four holes filled with solid water inserts. Another set of five cylindrical inserts was scanned in two phantoms (Model 002H5 and Model 002HN; CIRS Inc., Norfolk, VA, USA) with different sizes, but both made with identical water equivalent material [Fig. 2(b)]. The inserts consist of tissue mimicking material: lung (inhale), bone, muscle, adipose (product 002ED, CIRS Inc., Norfolk VA) and plastic water (002RW-S, CIRS Inc., Norfolk VA). Table II presents the density,  $\rho_e$ , and  $Z_{eff}$  of the Gammex RMI 467 and the CIRS tissue inserts (more detail can be found in Tables I and II of Landry et al.<sup>9</sup>). A Catphan 504 phantom (The Phantom Laboratory, Salem, NY, USA) consisting of several modules was also scanned with the same settings to

TABLE I. Scanner voltage pairs, pitch, exposure and rotation times for a combined computed tomography dose index (CTDI<sub>vol</sub>) of approximately 10 mGy, 20 mGy, and the maximum dose allowed by the scanner control software. The data for the three dose levels are separated by a semicolon for the CTDI<sub>vol</sub>, exposure and rotation time. 512 × 512 images were reconstructed for 3 mm slices with filtered back projection (FBP) and advanced modeled iterative reconstruction (ADMIRE) or with sinogram affirmative iterative reconstruction (SAFIRE).

	EDGE	FLASH	FORCE
Voltage pair (kVp)	120Au/120Sn	80/140Sn	90/150Sn
Pitch	0.3	0.6	0.7
CTDI <sub>vol</sub> (mGy)	9.97; 19.64; 44.12	9.99; 20.02; 40.85	9.99; 20.02; 65.42
Exposure (mAs)	468; 936; 2088	260/100; 530/205; 1083/418	199/124; 398/249; 1304/815
Rotation time (s)	0.33; 0.5; 1	0.28; 0.5; 1	0.28; 0.5; 1
Software version	VA49	VA48	VA50
Reconstruction	FBP and ADMIRE	FBP and SAFIRE	FBP and ADMIRE
Kernel	B40 and Q34 <sup>a</sup>	B40 and Q34	Br40 and Qr40 <sup>b</sup>

<sup>a</sup>The kernel nomenclature from the iterative reconstruction was recently redefined, in which the old Q34 is equivalent to the new Qr40 with beam-hardening correction for bone and the old B40 is equivalent to the new Br40.

<sup>b</sup>Qr40 with beam-hardening correction for bone selected.

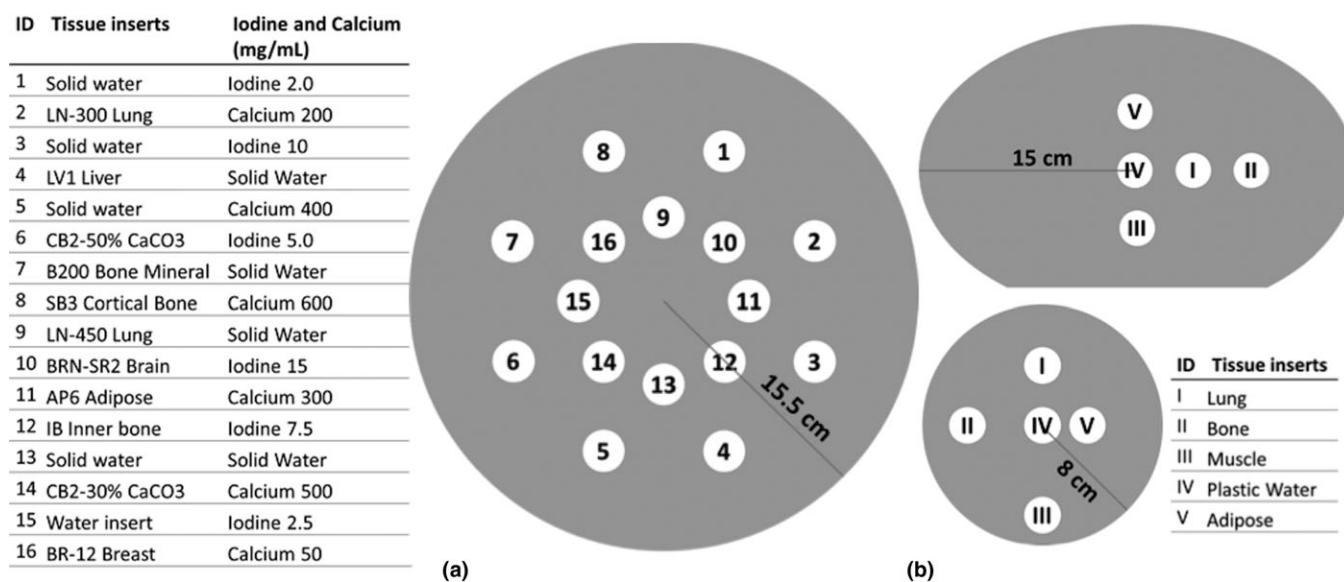


FIG. 2. (a) Sketch of the Gammex RMI 467 scans with the respective load pattern with tissue mimicking inserts and with iodine and calcium inserts. (b) Sketch of the CIRS abdomen (top) and head sized (bottom) phantoms with respective insert load pattern. Not to scale.

test image quality in terms of low contrast resolution of the axial plane.

The EDGE scanner has a minimum object width requirement of 10 cm in the cranial-caudal direction, since the reconstruction is unreliable within 3 cm from the edges. This is due to the combination of the twin-beam design and the use of a flat object. On the one hand, due to penumbra effects a few detector rows close to the boundary of the filtered beams see a mixture of both Au and Sn spectra. These detector rows are considered in the computation of the average image, but not for the dual-energy evaluations. On the other hand, the use of flat objects causes the attenuation to change drastically in the flat-edges, which has an impact in the data processing and

image quality. Our phantom, the Gammex RMI 467 phantom has a width of only 5 cm and its inserts have a length of 7 cm. For both these reasons, scans were made using two original 5 cm disks facing each other, thus assembling into a 10 cm wide phantom.

The Gammex RMI 467 scans using tissue mimicking inserts were used to calibrate each scanner for  $Z_{eff}$  and  $\rho_e$  (following Saito et al.<sup>8</sup> and Landry et al.<sup>9</sup>), whereas scans with the CIRS head and abdomen sized phantoms were used for validation. CT numbers in Hounsfield Units (HU) from the low- and high-energy images were measured in circular regions of interest (ROIs) that covered the inserts, avoiding their edges, in a selected central slice of each phantom.

TABLE II. Density ( $\rho$ , in  $\text{g/cm}^3$ ), relative electron density ( $\rho_e$ ) and effective atomic number ( $Z_{\text{eff}}$ ) of the inserts of the Gammex RMI 467 and of the CIRS phantoms.  $\rho_e$  and  $Z_{\text{eff}}$  (explained in Section 2.E.) were calculated with the elemental compositions given by the manufacturers of both phantoms.

	Insert name	$\rho$ ( $\text{g/cm}^3$ )	$\rho_e$	$Z_{\text{eff}}$
Gammex RMI 467	LN-300 lung	0.3	0.29	7.55
	LN-450 lung	0.46	0.45	7.53
	AP6 adipose	0.947	0.93	6.21
	BR-12 breast	0.98	0.96	6.93
	Water insert	1	1.00	7.48
	CT solid water	1.022	0.99	7.74
	BRN-SR2 brain	1.051	1.05	6.09
	LV1 liver	1.096	1.06	7.74
	IB inner bone	1.134	1.09	10.42
	B200 bone mineral	1.152	1.10	10.42
	CB2-30% CaCO <sub>3</sub>	1.331	1.28	10.90
	CB2-50% CaCO <sub>3</sub>	1.559	1.47	12.54
	SB3 cortical bone	1.822	1.69	13.64
CIRS	Lung	0.21	0.20	7.24
	Adipose	0.967	0.96	6.44
	Plastic water DT	1.039	1.00	7.55
	Muscle	1.062	1.04	7.59
	Bone	1.6	1.51	11.90

## 2.C. Spectral separation and CNR

DECT scans were reconstructed with iterative reconstruction (IR: SAFIRE and ADMIRE methods) and FBP of the iodine and calcium inserts in the Gammex RMI 467 phantoms from the three scanners. Merged images were obtained by mixing the low- and high-energy images with a weighted sum ( $w_{\text{low}} \cdot \text{CT}_{\text{low}} + w_{\text{high}} \cdot \text{CT}_{\text{high}}$ ), where the vendor-recommended weight factors for each scanner were used ( $w_{\text{low/high}}$ ). These images were then used to calculate the Contrast-to-Noise-Ratio (CNR) for each insert as

$$\text{CNR} = \frac{|\text{HU}_{\text{ROI}} - \text{HU}_{\text{surrounding}}|}{\text{Noise}}, \quad (1)$$

where  $\text{HU}_{\text{ROI}}$  and  $\text{HU}_{\text{surrounding}}$  are the mean values of CT numbers (in HU) in the ROI and the medium surrounding the insert. The noise is the standard deviation inside the ROI.

## 2.D. Quantification of image resolution

The CTP528 module from the Catphan phantom consists of 21 sets of aluminum strips separated by equally sized gaps, which are quantified in terms of line pairs per cm (lp/cm). The image resolution can be obtained using a Modulation Transfer Function (MTF) that describes the reduction in the contrast between the strips and the gaps as the number of line pairs per centimeter increases.<sup>20,21</sup> The MTF is calculated as

$$\text{MTF} = \frac{\text{Intensity}_{\text{strip}} - \text{Intensity}_{\text{gap}}}{\text{Intensity}_{\text{strip}} + \text{Intensity}_{\text{gap}}}, \quad (2)$$

where the intensities are measures of the CT numbers (HU). Spatial resolution is quantified when MTF equals 10% (expressed as @10%MTF). The MTF was calculated for both iterative reconstructed and FBP DECT images for each scanner.

## 2.E. Relative electron density ( $\rho_e$ ) and effective atomic number ( $Z_{\text{eff}}$ )

For quantitative imaging, the  $\rho_e$  and  $Z_{\text{eff}}$  were obtained from images reconstructed with ADMIRE (EDGE and FORCE) and SAFIRE (FLASH), this choice was based on Landry et al.<sup>16</sup> results showing improved accuracy of IR compared to FBP.

The  $\rho_e$  was derived using Saito's linear relation with respect to dual-energy subtracted CT numbers:<sup>8</sup>

$$\rho_e = a \cdot \frac{(1 + \alpha)\text{HU}_H - \alpha\text{HU}_L}{1000} + b, \quad (3)$$

where  $\text{HU}_L$  and  $\text{HU}_H$  are the mean values of CT numbers (in HU) in each ROI from the low- and high-energy images, respectively, and  $a$ ,  $b$ , and  $\alpha$  are scanner and protocol specific fit parameters.

The  $Z_{\text{eff}}$  was obtained using the relation formulated by Landry et al.<sup>9</sup> between the ratio of the attenuation coefficients ( $\mu$ ) for low- and high-energy, which resulted from the Rutherford et al.<sup>4</sup> parameterization of the linear attenuation coefficient as function of the scattering (coherent and incoherent) and the photoelectric effects. After converting the CT numbers into attenuation coefficients relative to water, the  $Z_{\text{eff}}$  equation is

$$\mu_{\text{High kVp}}^{\text{Low kVp}} = \frac{A + BZ_{\text{eff}}^{n-1} + CZ_{\text{eff}}^{m-1}}{D + EZ_{\text{eff}}^{n-1} + FZ_{\text{eff}}^{m-1}}, \quad (4)$$

where  $\mu_{\text{High kVp}}^{\text{Low kVp}}$  is the ratio between  $\mu_{\text{Low kVp,water}}^{\text{Low kVp}}$  and  $\mu_{\text{High kVp,water}}^{\text{High kVp}}$  and  $A$ ,  $B$ ,  $C$ ,  $D$ ,  $E$ ,  $F$ ,  $m$ , and  $n$  are fit parameters.  $A$ ,  $B$ , and  $C$  are terms related to the low energy kVp and  $D$ ,  $E$ , and  $F$  to the high energy kVp. The ratio  $\mu_{\text{Low kVp,water}}^{\text{Low kVp}}$  is defined as  $\mu_{\text{kVp}}/\mu_{\text{kVp,water}} = \text{HU}_{\text{kVp}}/1000 + 1$ .

Scans from the Gammex RMI 467 phantom were used to obtain the calibration fits (Eqs. 3 and 4) for each scanner and dose level. The values for atomic composition and mass density ( $\rho$ ) provided by the manufacturer were used to calculate the reference values of  $\rho_e = \rho \sum_i \frac{\omega_i Z_i}{A_i} / \rho_{e,\text{water}}$ , and  $Z_{\text{eff}} = \sqrt[n]{\sum_i \frac{\omega_i Z_i}{A_i} Z_i^n / \sum_i \frac{\omega_i Z_i}{A_i}}$ , where  $\omega$  is the relative weight of each element,  $Z$  is the atomic number,  $A$  is the atomic mass,  $\rho_{e,\text{water}}$  is the electron density of water and the exponent value  $n$  was set to 3.3.<sup>7</sup>

## 2.F. Comparison analysis

Experimental based estimations of  $\rho_e$ , and  $Z_{\text{eff}}$  were compared with reference values and the relative mean errors were

calculated. Accuracy was also calculated for the CIRS abdomen and head sized phantom scans.

The same quantities were obtained using *syngo.via* software (Siemens Healthineers, Forchheim, Germany) from which  $Z_{eff}$  and  $\rho_e$  images are extracted. The conversion of CT numbers to  $Z_{eff}$  and  $\rho_e$  are described in detail by Hünemohr et al.<sup>10</sup> The results from Saito and Landry et al.'s methods were compared with *syngo.via*, which can be found online (see Data S3).

### 3. RESULTS

Results are presented for the scans with a  $CTDI_{vol}$  of approximately 20 mGy, unless otherwise indicated.

#### 3.A. Spectral separation for iodine and calcium inserts

Figure 3 shows low-kVp and high-kVp CT numbers for the iterative reconstructed scans with different iodine and calcium inserts. Figure 3(a) presents the scatter plots for the twin-beam scanner EDGE, which are closer to the identity line (in black) than the plots for the dual-source scanners FLASH and FORCE [Figs. 3(b) and 3(c)]. Specifically, the iodine inserts present poorly separated CT numbers in Fig. 3(a). The difference between the two generation detectors is apparent in the scatter clouds' size, where the images acquired with third-generation digital detectors show a smaller variation in CT numbers [Fig. 3(a) and 3(c)].

Figure 4 presents the CNR for the iodine [Fig. 4(a)] and the calcium [Fig. 4(b)] inserts for the FBP scans of the three scanners. Both figures show the results for  $CTDI_{vol}$  of approximately 10 mGy and 20 mGy. Both figures show higher values of CNR for the FORCE scanner. Although the EDGE has similar noise levels, the difference between the mean CT numbers and the surrounding are lower, resulting in a lower CNR. Similar values of CNR are found for the EDGE and the FLASH.

#### 3.B. Spatial resolution

Figure 5 shows the MTF as function of the frequency (in lp/cm) for the three scanners for a  $CTDI_{vol}$  of approximately 20 mGy for two different reconstructions: FBP and IR. Image resolution @10%MTF is 6.2 lp/cm, 5.8 lp/cm and 6.2 lp/cm for the iterative reconstructed images from the EDGE, FLASH, and FORCE scanners, respectively. Slightly inferior values are found for the FBP reconstructed images (6.1 lp/cm, 5.7 lp/cm, and 6 lp/cm). Values for @10%MTF are constant for the three dose levels used ( $\pm 0.1$  lp/cm).

#### 3.C. Calibration of $\rho_e$ and $Z_{eff}$ for each scanner

For the assessment of  $\rho_e$  and  $Z_{eff}$ , iterative reconstructed scans were used (see Data S1).

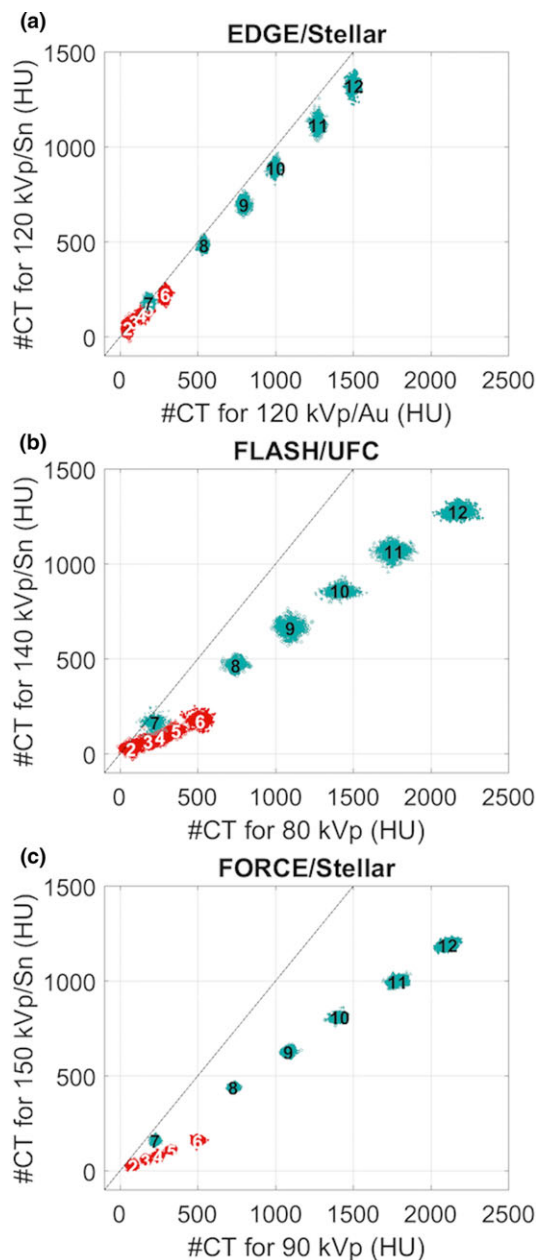


FIG. 3. Low and high energy #CT plots for the iodine (2, 2.5, 5, 7.5, 10, and 15 mg/ml) and calcium (50, 200, 300, 400, 500, and 600 mg/ml) inserts for  $CTDI_{vol}$  of approximately 20 mGy for the EDGE (a), FLASH (b), and FORCE (c) scanners. Inserts are numbered from low to high density, in which the iodine inserts have numbers 1 to 6 (iodine 2 mg/ml and 2.5 mg/ml overlap) and the calcium inserts are numbered from 7 to 12. The identity line is plotted in black and each scatter point corresponds to one pixel from each insert's ROI. [Color figure can be viewed at [wileyonlinelibrary.com](http://wileyonlinelibrary.com)]

Saito's calibration fit parameters are presented in Table III. The parameter  $\alpha$  should be smaller for larger spectral separation (see Saito's eq. 3<sup>8</sup>). The calibration fits for  $Z_{eff}$  as a function of the ratio of the attenuation coefficients ( $\mu_{High\ kVp}^{Low\ kVp}$ ) are shown in Fig. 6. The Gammex RMI 467 phantom lung equivalent inserts were excluded from the fitting procedure, as reported also by Landry et al.,<sup>7</sup> since they are heterogeneous and their low CT numbers lead to high standard deviation

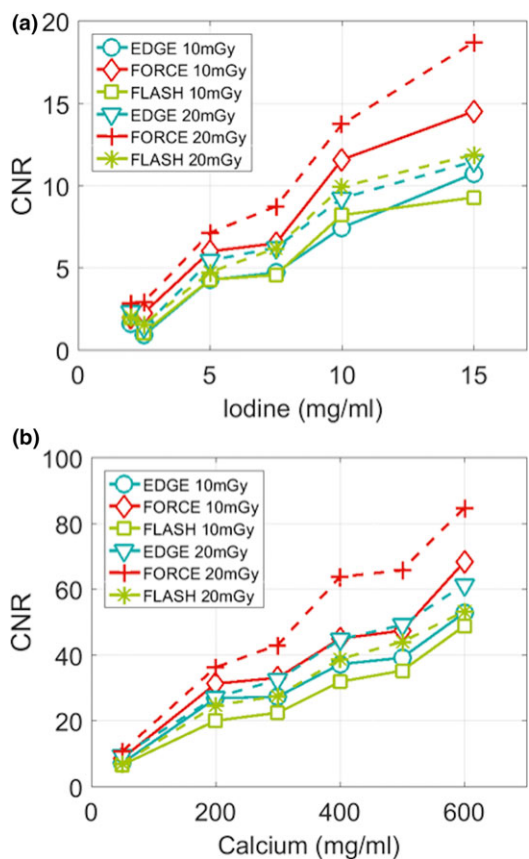


FIG. 4. Contrast-to-Noise-Ratio (CNR) for the iodine (a) and calcium (b) inserts for two CTDI<sub>vol</sub> of approximately 10 mGy (solid) and 20 mGy (dashed line). [Color figure can be viewed at wileyonlinelibrary.com]

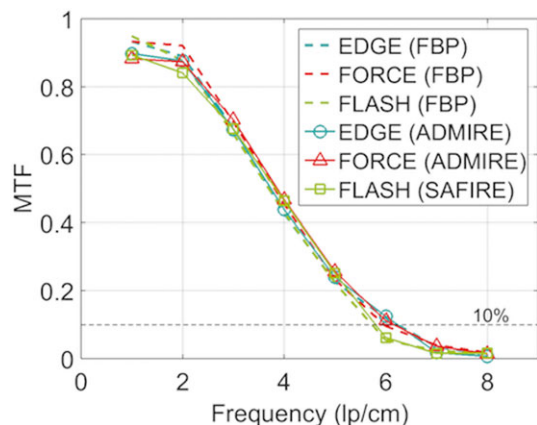


FIG. 5. Modulation Transfer Function (MTF) for the three DECT scanners at a CTDI<sub>vol</sub> of approximately 20 mGy. [Color figure can be viewed at wileyonlinelibrary.com]

TABLE III. Saito’s fit parameters  $a$ ,  $b$ , and  $\alpha$  from Eq. (3) for the calibration phantom Gammex RMI 467.

	EDGE	FLASH	FORCE
$\alpha$	2.06	0.44	0.35
$a$	1.04	0.98	0.99
$b$	0.99	0.99	0.99

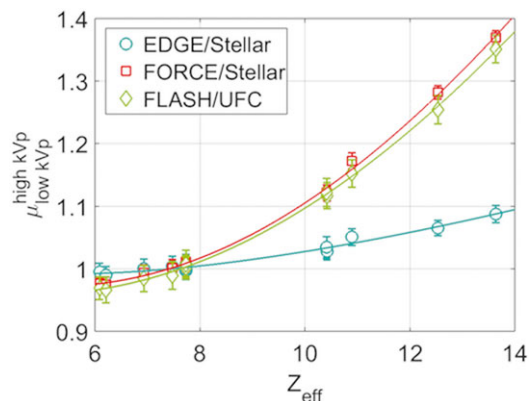


FIG. 6. Fit results for Eq. (4) using the Gammex RMI 467 phantom with tissue mimicking inserts at equivalent dose. Both lung inserts were excluded from the fitting procedure. Error bars are the standard deviations for each insert. [Color figure can be viewed at wileyonlinelibrary.com]

values. The interval range of  $\mu_{High\ kVp}^{Low\ kVp}$  differs between the twin-beam scanner,  $\sim 0.1$  and the dual-source scanners,  $\sim 0.4$  (Fig. 6).

### 3.D. Errors of measured $\rho_e$ and $Z_{eff}$

The errors of  $\rho_e$  and  $Z_{eff}$  for the calibration (Gammex RMI 467) and validation phantoms (CIRS abdomen and head size) are shown in Fig. 7. In Figs. 7(a) and 7(b) a pattern is identified: the errors from the EDGE are higher for the inserts in the inner ring of the phantom. For the dual-source scanners FLASH and FORCE, the errors for  $\rho_e$  range between  $[-0.6\%, 1.2\%]$  and  $[-1.2\%, 0.4\%]$ , and for  $Z_{eff}$  between  $[-6.2\%, 3.8\%]$  and  $[-5.2\%, 1.6\%]$ . For the twin-beam scanner, the errors have wider ranges:  $[-0.7\%, 15.3\%]$  for  $\rho_e$  and  $[-28.1\%, 4.2\%]$  for  $Z_{eff}$ .

Figures 7(c) and 7(d) show the errors of  $Z_{eff}$  and  $\rho_e$  for the two validation phantoms. Relative differences between  $\rho_e$  values of the same insert in the two different phantoms are within 0.6% for the FLASH and EDGE, with the exception of the lung insert, whereas for the FORCE scanner all relative differences are within 0.5%. For  $Z_{eff}$ , discrepancies are observed in lung and adipose for the EDGE scanner (14.5% and 6.9%) and also in adipose for the FORCE scanner (5.6%). All other relative differences between  $Z_{eff}$  are within  $\pm 2\%$ .

### 3.E. Material attribution feasibility

Tissue composition segmentation can be done with the  $[\rho_e, Z_{eff}]$  space (detailed in section 2.5 from Landry et al.<sup>7</sup>), which uses the two-dimensional Mahalanobis distance to assign each voxel to its closest reference material. For this method to be feasible, a proper separation in the  $[\rho_e, Z_{eff}]$  space of the scatter plots for the different calibration materials should exist. Figure 8 presents the scatter plots from the scans with the calibration phantom for the three scanners. The data discretization observed for low  $Z_{eff}$  values (e.g., for the lung tissues) are a result of saving CT numbers’ as integers by the vendors’ software. In Fig. 8(a1), it is possible to

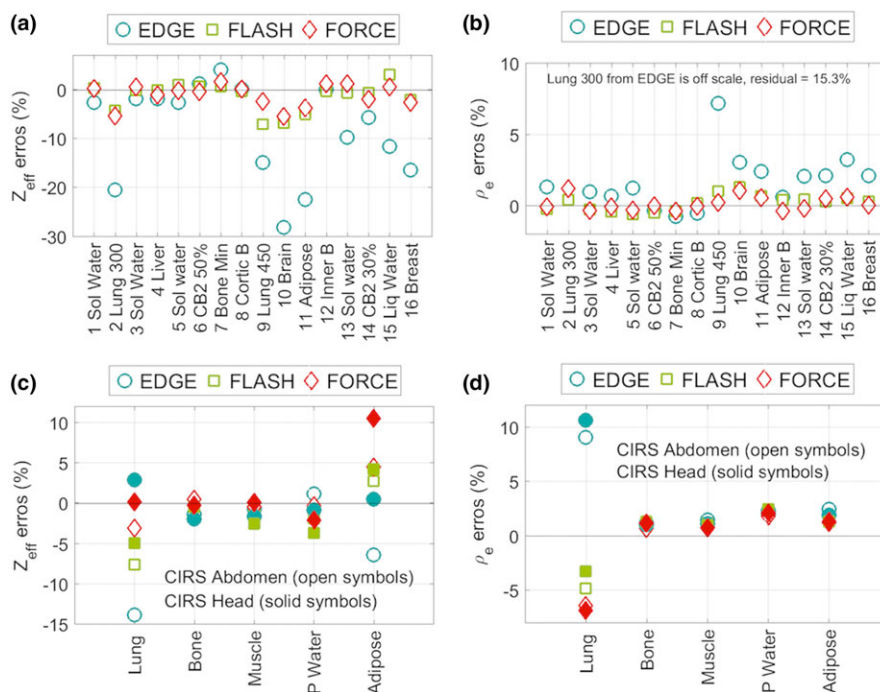


FIG. 7.  $\rho_e$  and  $Z_{eff}$  errors (%) of measured values with respect to reference values of the Gammex RMI 467 phantom (a and b) and the CIRS abdomen and head sized phantoms (c and d). [Color figure can be viewed at wileyonlinelibrary.com]

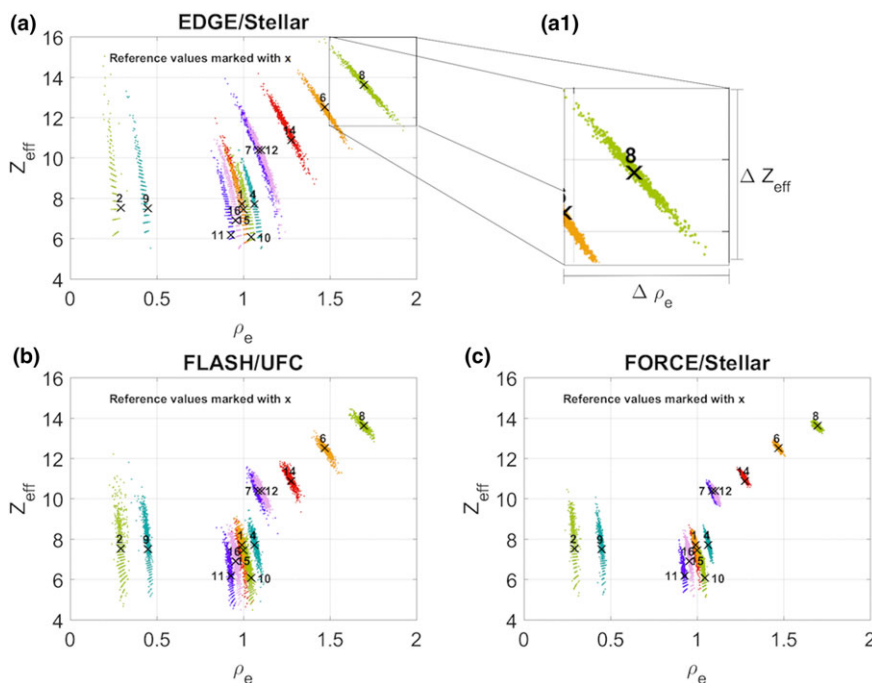


FIG. 8. (a) EDGE, (b) FLASH, and (c) FORCE [ $\rho_e$ ,  $Z_{eff}$ ] scatter plots of the Gammex RMI 467 calibration phantom (CTDI<sub>vol</sub> of approximately 20 mGy). (a1) shows the scatter plot for the cortical bone insert (insert number 8), where the spread on  $\rho_e$  and  $Z_{eff}$  are identified with  $\Delta\rho_e$  and  $\Delta Z_{eff}$ . The inserts are numbered according to Fig. 2(a). The solid water inserts 3, 5, and 13 were excluded from these plots, since they did not add any extra information. [Color figure can be viewed at wileyonlinelibrary.com]

observe in detail the cortical bone insert (insert number 8) for the EDGE scanner, which shows the spread of  $\rho_e$  ( $\Delta\rho_e$ ) and  $Z_{eff}$  ( $\Delta Z_{eff}$ ). Compared to the other two scanners, these ranges are wider for all inserts in the EDGE, which is especially noticeable for the bone tissues.

All voxels from the lung and hard bone equivalent tissue were assigned to the correct material for the Gammex RMI 467 phantom (see Data S2). The inner bone and bone mineral equivalent inserts have similar compositions and density, resulting in very close values of  $\rho_e$  and  $Z_{eff}$  (Fig. 8).<sup>11</sup> The

visible overlap of the soft tissues results in lower percentage of correct material attribution, which can be improved with lower spread of the  $[\rho_e, Z_{eff}]$  clouds. The CIRS tissue inserts are well separated in the  $[\rho_e, Z_{eff}]$  space resulting in 100% correct material attribution, except for muscle and plastic water in the abdomen size phantom for the EDGE scanner (93% and 98%, respectively). The errors of the  $\rho_e$  and  $Z_{eff}$  as well as the scatter plots of the  $[\rho_e, Z_{eff}]$  space were obtained from the  $\rho_e$  and  $Z_{eff}$  images extracted from *syngo.via* (see Data S3).

#### 4. DISCUSSION

The novel technology presented in this paper, the split-filter from the EDGE scanner, has the advantage of using a single x-ray tube to do DECT scans, allowing for a possible upgrade on many clinical SECT scanners. In this work, a comparison of this new technique with the state-of-the-art dual-source DECT scanners was done to assess the performance of the twin-beam on quantitative imaging, knowing beforehand that the spectral separation of the twin-beam would not be as good as the one from the dual-source DECT scanners.

The twin-beam scanner has a width requirement of 10 cm in the craniocaudal direction, as explained in the section Material and Methods. Although the scans with the calibration phantom were made using two Gammex RMI 467 disks, it is important to point out that using the *syngo.via* software, non-uniform  $Z_{eff}\rho_e$  images along the phantom's profile were obtained for uniform inserts, whereas such non-uniformities were not seen in the CIRS phantoms, which have a width of 15 cm. Even then, the central slice of the Gammex RMI 467 disk with the inserts presented the most uniformly reconstructed image and it was used to perform the calibration.

A consequence of the twin-beam energy spectra [Fig. 1(a)] is the poor CT number separation seen in Fig. 3(a) for the iodine and calcium inserts. The two dual-source scanners, with well-separated spectra, present a noticeable distinction in CT numbers between the low and high energy scans for the iodine and calcium scans. The FORCE scanner with the third-generation detectors and the smaller spectral overlap (of only 10.5% of the area overlapping) shows scatter plots further away from the identity line and with lower variations.

The FLASH and EDGE have similar CNR results for both iodine and calcium materials. On one hand, the second generation dual-source scanner FLASH has a good contrast due to its wider spectral separation, but higher noise levels due to the detector. On the other hand, the split-beam scanner EDGE has low noise values, but also low contrast due to its narrower spectral separation. The FORCE has a CNR on average 1.5 times superior to the FLASH and 1.4 superior to the EDGE.

In terms of image resolution, the results for the @10% MTF are similar for both the EDGE and the FORCE scanners and slightly lower for the FLASH, since this is mostly related with the detectors' system.

The calibration of  $\rho_e$  and  $Z_{eff}$  was performed for the three scanners using the methods from Saito et al.<sup>8</sup> and Landry

et al.<sup>9</sup> The EDGE presented less robust calibration curves with higher fit residuals. This can be explained again by the reduced spectral separation of the twin-beam, that resulted in a high  $\alpha$  parameter for the  $\rho_e$  fit (Table III) and a low range of the attenuation coefficients ratio for the  $Z_{eff}$  fit [Fig. 6(a)]. These results have a direct implication on the extraction of the  $\rho_e$  and  $Z_{eff}$ , which had overall higher differences with the reference values and spread out clouds in the  $[\rho_e, Z_{eff}]$  scatter plots for this scanner. The same or higher deviations were obtained from *syngo.via*'s images, which use a different method to calculate  $\rho_e$  and  $Z_{eff}$ .

The  $\rho_e$  and  $Z_{eff}$  errors for the calibration phantom are noticeably higher for the EDGE, especially for all inserts located in the inner ring of the Gammex RMI 467 phantom [inserts 9 to 16, Figs. 7(a) and 7(b)]. This can be related to the twin-beam requirement to reconstruct objects thicker than 10 cm. For this phantom, the FLASH and the FORCE scanners presented lower errors for the tissue substitute inserts, specifically, errors for the soft tissues within 1.3% for  $\rho_e$  and 7% for  $Z_{eff}$  and for the bone tissues within 0.5% for  $\rho_e$  and 1.9% for  $Z_{eff}$ .

The validation was performed with a different set of tissue-equivalent inserts in two different sized phantoms, aiming also to assess the robustness of the calibration for a smaller phantom. Values of  $\rho_e$  for both phantoms have a relative difference within 0.6% for the three scanners. Higher discrepancies are observed for  $Z_{eff}$ , within 2% for bone, muscle and water and within 6% for adipose. From these results, it is possible to conclude that the calibration methods used for DECT are not phantom-size dependent, as long as beam-hardening effects are corrected during the image reconstruction.

Images acquired with the twin-beam technology resulted in widely spread  $\rho_e$  and  $Z_{eff}$  (Fig. 8) values for the same material type, contrary to the results from the dual-source scanners. The use of different IR algorithms and detector systems and the lack of performance from the lung equivalent inserts are limitation from this study, but these do not change its overall conclusions.

#### 5. CONCLUSION

The dual-source scanners measure  $\rho_e$  and  $Z_{eff}$  values closer to the reference ones, when compared with the twin-beam scanner, with a higher accuracy for the third-generation scanner FORCE. The dual-source third-generation scanner resulted in higher resolution and CNR than the other two scanners.

A comparison study between a scanner with a novel DECT technique, a split-beam, and dual-source DECT scanners is shown in this paper. Understanding the implications of using this new technique in terms of resolution, contrast and derivation of two quantities,  $\rho_e$  and  $Z_{eff}$ , seemed essential to assess the future of the twin-beam scanner for radiotherapy with photon and ion beams. The contrast and tissue material segmentation are necessary for a better contouring of body structures, organs and tumors. Also, an accurate calculation

of these quantities is necessary to perform dose calculations and to be able to do *in vivo* range prediction for treatment verification for particle therapy. Finally, other features in quantitative imaging such as detailed texture analysis show the need for high-quality DECT images.

## ACKNOWLEDGMENTS

We thank Dr Bernhard Schmidt from Siemens Healthineers for the opportunity to use the SOMATOM Definition EDGE with the twin-beam dual-energy technology in the Siemens factory (Forchheim, Germany). Drs Bernhard Krauss, Bernhard Schmidt, and Nora Hunemöhr from Siemens Healthineers are acknowledged for their valuable comments on this work. Dr Marco Das and Ralph Eschweiler from the Academic Hospital, Maastricht, are acknowledged for providing the time slots with both dual-source scanners. We would like to thank Jef Willigers for the help with the measurements at the Academic Hospital, Maastricht.

<sup>a)</sup>Author to whom correspondence should be addressed. Electronic mail: frank.verhaegen@maastro.nl; Telephone: +31 (0)88 4455792.

## REFERENCES

1. Fletcher JG, Leng S, Yu L, McCollough CH. Dealing with uncertainty in CT images. *Radiol.* 2016;279:5–10.
2. Mileto A, Barina A, Marin D, et al. Virtual monochromatic images from dual-energy multidetector CT: Variance in CT numbers from the same lesion between single-source projection-based and dual-source image-based implementations. *Radiol.* 2016;1:269–277.
3. van Elmpt W, Landry G, Das M, Verhaegen F. Dual energy CT in radiotherapy: current applications and future outlook. *Radiother Oncol.* 2016; doi:10.1016/j.radonc.2016.02.026.
4. Rutherford RA, Pullan BR, Isherwood I. Measurement of effective atomic number and electron density using an EMI scanner. *Neuroradiol.* 1976;11:15–21.
5. Bazalova M, Verhaegen F. Dual-energy CT-based material extraction for tissue segmentation in Monte Carlo dose calculations. *Phys Med Biol.* 2008;53:2439–2456.
6. Landry G, Reniers B, Granton PV, et al. Extracting atomic numbers and electron densities from a dual source dual energy CT scanner: experiments and a simulation model. *Radiother Oncol.* 2011;100:375–379.
7. Landry G, Granton PV, Reniers B, et al. Simulation study on potential accuracy gains from dual energy CT tissue segmentation for low-energy brachytherapy Monte Carlo dose calculations. *Phys Med Biol.* 2011;56:6257–6278.
8. Saito M. Potential of dual-energy subtraction for converting ct numbers to electron density based on a single linear relationship. *Med Phys.* 2012;39:2021–2030.
9. Landry G, Seco J, Gaudreault M, Verhaegen F. Deriving effective atomic numbers from DECT based on parameterization of the ratio of

- high and low linear attenuation coefficients. *Phys Med Biol.* 2013;58:6851–6866.
10. Hünemöhr N, Krauss B, Tremmel C, Ackermann B, Jakel O, Greilich S. Experimental verification of ion stopping power prediction from dual energy CT data in tissue surrogates. *Phys Med Biol.* 2014;59:83–96.
  11. Mahnken AH, Stanzel S, Heismann B. Spectral pZ-projection method for characterization of body fluids in computed tomography. *Acad Radiol.* 2009;26:763–769.
  12. Yu L, Leng S, McCollough CH. Dual-energy CT-based monochromatic imaging. *AJR Am J Roentgenol.* 2012;199:S9–S15.
  13. Euler A, Parakh A, Falkowski AL, et al. Initial results of a single-source dual-energy computed tomography technique using a split-filter assessment of image quality, radiation dose, and accuracy of dual-energy applications in an *In Vitro* and *In Vivo* study. *Invest Radiol.* 2016;51:491–498.
  14. Flohr TG, Leng S, Yu L, et al. Dual-source spiral CT with pitch up to 3.2 and 75 ms temporal resolution: image reconstruction and assessment of image quality. *Med Phys.* 2009;36:5641.
  15. Christe A, Heverhagen J, Ozdoba C, Weisstanner C, Ulzheimer S, Ebner L. CT dose and image quality in the last three scanner generations. *World J Radiol.* 2013;5:421–429.
  16. Landry G, Gaudreault M, van Elmpt W, Wildberger JE, Verhaegen F. Improved dose calculation accuracy for low energy brachytherapy by optimizing dual energy CT imaging protocols for noise reduction using sinogram affirmed iterative reconstruction. *Med Phys.* 2015;26:75–87.
  17. Poludniowski GG, Evans PM. Calculation of x-ray spectra emerging from an x-ray tube. Part I. electron penetration characteristics in x-ray targets. *Med Phys.* 2007;34:2164–2174.
  18. Poludniowski GG. Calculation of x-ray spectra emerging from an x-ray tube. Part II. X-ray production and filtration in x-ray targets. *Med Phys.* 2007;34:2175–2186.
  19. Poludniowski GG, Landry G, DeBlois F, Evans PM, Verhaegen F. SpekCalc: a program to calculate photon spectra from tungsten anode x-ray tubes. *Phys Med Biol.* 2009;54:433–438.
  20. Takenaga T, Katsuragawa S, Goto M, Hatemura M, Uchiyama Y, Shiraiishi J. Modulation transfer function measurement of CT images by use of a circular edge method with a logistic curve-fitting technique. *Radiol Phys Technol.* 2015;8:53–59.
  21. Friedman SN, Fung GSK, Siewerdsen JH, Tsui BMW. A simple approach to measure computed tomography (CT) modulation transfer function (MTF) and noise-power spectrum (NPS) using the American College of Radiology (ACR) accreditation phantom. *Med Phys.* 2013;40:051907.

## SUPPORTING INFORMATION

Additional Supporting Information may be found online in the supporting information tab for this article.

**Data S1.** Gammex RMI 467 scanned with the twin-beam scanner EDGE.

**Data S2.** Correctness of material assignment for Gammex RMI 467.

**Data S3.** Comparison with *syngo.via*.